In-lab calibration and testing of adaptive secondary mirrors using phase measuring deflectometry

Ruihan Zhang, Mark Chun

Ruihan Zhang, Mark R. Chun, "In-lab calibration and testing of adaptive secondary mirrors using phase measuring deflectometry," Proc. SPIE 12185, Adaptive Optics Systems VIII, 1218569 (29 August 2022); doi: 10.1117/12.2627278

SPIE.

Event: SPIE Astronomical Telescopes + Instrumentation, 2022, Montréal, Québec, Canada

In-Lab Calibration and Testing of Adaptive Secondary Mirrors Using Phase Measuring Deflectometry

Ruihan Zhang[a] and Mark R. Chun[a]

[a]Institute for Astronomy, University of Hawai'i at Hilo, 640 N Aohoku Pl, Hilo, USA

ABSTRACT

An adaptive secondary mirror (ASM) with novel actuator technology is being designed and built for the UH88 telescope as a demonstration of a new generation of ASMs that might be deployed at ground based observatories such as Keck, Subaru, and TMT. Before putting the ASM on the telescope, a set of calibrations and characterizations need to be made in the lab. The crucial lab characterizations of the ASM are to measure its influence functions, and its surface shape when powered and unpowered. To measure these, we develop a novel and inexpensive optical metrology approach using phase measuring deflectometry. This paper describes the simulations we wrote to model the deflectometry method, our data acquisition/analysis pipeline, and a lab prototype system we built that demonstrates its feasibility on a microelectromechanical systems (MEMS) deformable mirror. Based on the information gained through the deflectometry simulation and the setup prototype, we conclude that phase measuring deflectometry is a reasonable method for obtaining the influence functions but that the absolute surface shape of the ASM will be limited by our knowledge of the placement of components within the deflectometry setup itself. We discuss challenges with extending this approach to larger convex adaptive secondary mirrors.

Keywords: Adaptive Optics, Adaptive Secondary Mirrors, Phase Measuring Deflectometry, Optical Metrology

1. INTRODUCTION

Deformable mirrors (DMs) come in different flavors, including small micro-optical-electrical-mechanical systems (MEMS), medium-sized piezo DMs, and large adaptive secondary mirrors (ASM).[1] We focus our attention on ASMs which can provide a corrected wavefront for all instruments on the telescope. ASM technologies have advanced rapidly in the past few years and several world-class telescopes are now using them, including the Large Binocular Telescope (LBT),[2] the ESO VLT-UT4,[3] the Multiple Mirror Telescope,[4] and the Magellan Telescope.[5]

The main advantages of an ASM-based AO system are its low thermal emissivity, its high optical throughput, and its ability to provide a wide corrected field of view. Others (c.f. Lloyd-Hart[4]) have illustrated the advantages for observations at thermal infrared wavelengths (e.g. $> 2.2\mu$m) of an ASM-based AO system compared to conventional AO systems with a "warm" optical relay and a conventional DM. The reduction of the thermal background can lead to observing efficiency gains of factors of 2-3 over conventional AO systems for background-limited observations. These advantages are especially pronounced in high altitude observing sites, like Mauna Kea, where the air is dry and the emission of water vapor is low.

The second substantial gain for an ASM-based AO system is that the ASM enables large partially corrected fields of view for all instruments on the telescope. Achieving a wide field of view for a conventional AO system is challenging because it is difficult to produce an optical relay with a wide field of view and high-quality pupil and focal planes. An ASM provides a natural way to do this. The wide-field partial correction is particularly attractive to sites that have weak turbulence in the free atmosphere and highly confined ground/surface layers.[6–8] Gemini observatory has performed a feasibility study on employing Ground-layer adaptive optics (GLAO) with

Further author information: (Send correspondence to R.Z.)
R.Z.: E-mail: rzhang9@hawaii.edu, Telephone: 1 309 531 3014
M.R.C.: E-mail: markchun@hawaii.edu, Telephone: +1 808 934 7003

Adaptive Optics Systems VIII, edited by Laura Schreiber, Dirk Schmidt, Elise Vernet,
Proc. of SPIE Vol. 12185, 1218569 · © 2022 SPIE
0277-786X · doi: 10.1117/12.2627278

an ASM and its benefits. Szeto et al. (2006) find that GLAO will bring: "improved, uniform, image quality at all wavelengths over large fields (∼10') through compensation for both telescope vibrations and ground-layer atmospheric effects; [increased] productivity since the currently best 20%-ile seeing will occur 80% of the time and the poorest image quality will be improved to average image quality; new science capabilities: high Strehl mid-IR science, wide field imaging projects that require excellent image quality to be feasible, and multiplexed deployable integral field spectroscopy".[9] Similar studies have been done for the ULTIMATE-Subaru project with wide-field GLAO.[10] The Subaru team also report there will be significant improvements in the image quality over a wide field-of-view if an ASM is deployed, which will enable high-redshift galaxy surveys and other science cases.

Despite all their benefits, current ASMs have their disadvantages. They are complex/costly and existing ASMs have been difficult to operate and maintain in practice.[11] For these reasons, our team, in collaboration with three industrial partners (TNO, VDL, and Hyperion), is developing a new ASM for the University of Hawaii 2.2-meter telescope (UH88)[12,13] using a novel actuator technology developed by TNO. The new actuators have a larger force output and lower heat dissipation which should lead to a simpler and more robust ASM with less thermal contamination.[14]

The ASM is expected to be delivered to Hawaii in summer 2023 and we will be performing in-lab tests and calibrations using a variety of optical tests. There are two key measurements that we will make before putting the ASM on-sky: (1) obtain the influence functions of the ASM, and (2) measure the unpowered and powered surface shape of the ASM. The influence functions describe how the surface shape of the ASM changes when commands are applied to its actuators. Based on the measured influence functions, the ASM is driven to desired shapes to correct for the atmospheric aberrations. The unpowered, or the natural, surface shape of the ASM is important because it defines (1) what wavefront errors the actuators need to take out in order for the ASM to assume the correct shape for the optics of the telescope and (2) what aberrations in the facesheet are beyond the ability of the actuators to correct. Both measurements quantify the "static" performance limits of the ASM. Hence, in this project we develop a measurement method for the ASM using a relatively new optical metrology approach called phase measuring deflectometry (PMD). This approach is similar to the approach used in commercial 3D scanners and has recently been applied to testing optical surfaces.[15] In the next section, we will briefly explore why we choose PMD as the measurement method for the ASM.

1.1 Why Phase Measuring Deflectometry

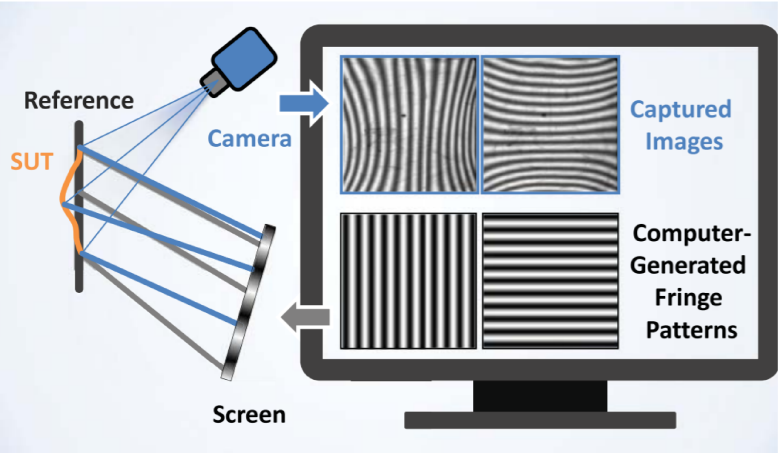

Figure 1. The basic principle of phase measuring deflectometry that uses a screen and a camera to measure the shape of the surface under test (SUT). Image credit: Huang et al. 2018.[15]

Metrology tests for convex mirrors are inherently difficult because the absence of a real focus. This results in the need for optics in the test setup that are as large or larger than the surface under test. For example, the use of a classical Hindle sphere mirror to test the UH88's convex hyperboloid secondary mirror would require a spherical mirror 2-3 meters in diameter. The ESO setup for testing its adaptive secondary mirror, ASSIST, cost

over 2.5 million euros.[16] The situation becomes even more intractable when one considers what the test setup would look like for a 3-m diameter ASM for an ELT such as TMT. For our ASM project, we are exploring a number of alternative approaches to measure the mirror surface. This project focuses on a novel technique called Phase Measuring Deflectometry (PMD).

Phase measuring deflectometry is an optical metrology technique that retrieves the 3D shape of an object, in our case the surface of a mirror, by measuring how a known pattern gets distorted when reflected off the mirror surface as shown in Fig. 1.[15] It employs the law of reflection to ray-trace "pixel-by-pixel" from the pattern displayed on an LCD screen to the mirror surface to a camera that records the reflected image. The mapping between the pixels located on the screen and the pixels on the captured images depends on the location of the three elements (screen, mirror, camera) and the shape of the mirror surface, specifically the slope of the surface. Using simple geometry, the surface slopes can be calculated by comparing the captured/distorted fringe patterns to the original fringe patterns.

On a practical perspective, the equipment needed for PMD is simple to obtain and put together, which consists of mostly commercially available LCD screens and cameras. PMD is several orders of magnitude less expensive than conventional interferometric approaches, which are typically used for large convex aspheric mirrors like the UH88 ASM. If PMD proves to be a reasonable method for measuring the influence functions and surface shape of the UH88 ASM, we may be able to scale up the setup by using movie theater projection screens or multiple LCD screens to perform tests for larger ASMs in the future.

There are also challenges to using PMD. PMD depends critically on knowledge of the geometry of the screen, camera, and mirror setup and distortions in the system (e.g. camera lens distortions). Hence uncertainties and instabilities in any of these can lead to errors in the reconstructed surface. Nonetheless, a carefully calibrated PMD system can achieve sub-micron RMS surface measurements and PMD has been used to test the optical quality of several large telescope mirrors, such as DKIST and LBT.[17]

1.2 UH88 ASM Requirements on PMD

For the UH88 ASM project, the requirements on our PMD setup are rather loose. First, we need PMD to measure the influence functions for each actuator. This measurement is differential, which means it is a measurement of the change in surface shape due to a change in command on one of the actuators. Making a differential measurement means that we first measure the shape of the relaxed ASM, where all actuator are in their idle position with no current applied, and then measure the surface with one or more actuators are poked. The difference between the two measured shapes is our final measurement. As long as the setup is stable during the measurement of the idle state and the poked state, many of the uncertainties in the setup calibrations do not contribute to the differential measurement.

Moreover, the ASM will very seldom operate in "open loop" where we are fully dependent on the measured influence functions. Under most circumstances, the ASM will be controlled via optical feedback from a wavefront sensor. One scenario where this might not be the case is when the ASM is used as a static secondary mirror in support of instruments that do not have a wavefront sensor to monitor the shape. These instruments will be, by definition, seeing-limited so small errors in our applied static shape of the ASM will not greatly reduce the overall image quality. In this scenario the influence functions only need to be accurate enough so that the error in the wavefront is dominated by atmospheric aberrations instead of measurement error in the influence functions. To quantify how errors in the influence functions impact the wavefront correction, we performed a Monte-Carlo (MC) simulation (the simulation will be discussed in details in Section 3). The result of the MC simulation shows that knowing the influence functions to about 10-20% results in negligible errors in the expected static aberration correction of the telescope optical errors. We can quantify this error in physical units: the usual seeing-limited wavefront aberration detected at 500nm using a 2.2m telescope is roughly 1μm RMS based on Kolmogorov's atmospheric model,[18] 10% of that error is 0.1μm, which is the accuracy requirement that we adopt for our influence functions measurement using PMD.

Ideally PMD will also give us an estimate of the unpowered (and powered) surface shape of the ASM. In particular we need to estimate how closely we can command the ASM to a particular shape (e.g. the aspheric shape for the UH88 telescope). Given that the actuator range is +/- 15μm,[19] we aim to measure the low spatial

frequency shape of the ASM to a few microns. This is about an order of magnitude larger than the accuracy the previous studies have achieved using PMD.[17] In summary, the error tolerance for differential measurements are $\sim 0.1\mu$m and the error tolerance for the absolute measurement is $\sim 1\mu$m.

To study the feasibility of using PMD for the UH88 ASM project, we (1) wrote a simple ray-tracing simulation for the deflectometry setup and (2) developed a small scale lab prototype to test it with the a conventional deformable mirror. The simulation provided us a way to quantify the impact of measurement uncertainties and constraints. The lab prototype provided a context to develop the data acquisition/analysis pipeline and to start quantifying the real-world errors and calibrations. Using knowledge learned from the simulation and the prototype, we also developed a conceptual design of the PMD setup for testing the ASM. The following sections of the paper will cover basic PMD concepts and how it works, results gained from the ray-tracing simulation and the deflectometry prototype with the Robo-AO DM, and the initial design of the deflectometry setup for the ASM.

2. METHODOLOGY/FORMALISMS

Phase Measuring Deflectometry essentially measures how the gradient on the surface under test (SUT) deflects rays coming from the screen and reflecting into the camera. In practice this tracing of rays is accomplished by recording the reflected images of a series of sinusodial fringe patterns. The difference between the distorted fringe patterns and the non-distorted fringe patterns carry information about the slopes on the SUT. These slopes can then be integrated across the surface to retrieve the surface shape of the SUT. In this section, we will go into the mathematical details about how this process works, how we can retrieve the screen pixel to mirror position mapping using sinusoidal fringe patterns and eventually reconstruct the mirror wavefront.

A simple PMD setup consists of a camera, an LCD screen, a control computer, and a mechanical fixture that holds all of the elements in place with respect to the SUT. Fig. 2 shows what the general setup looks like. The

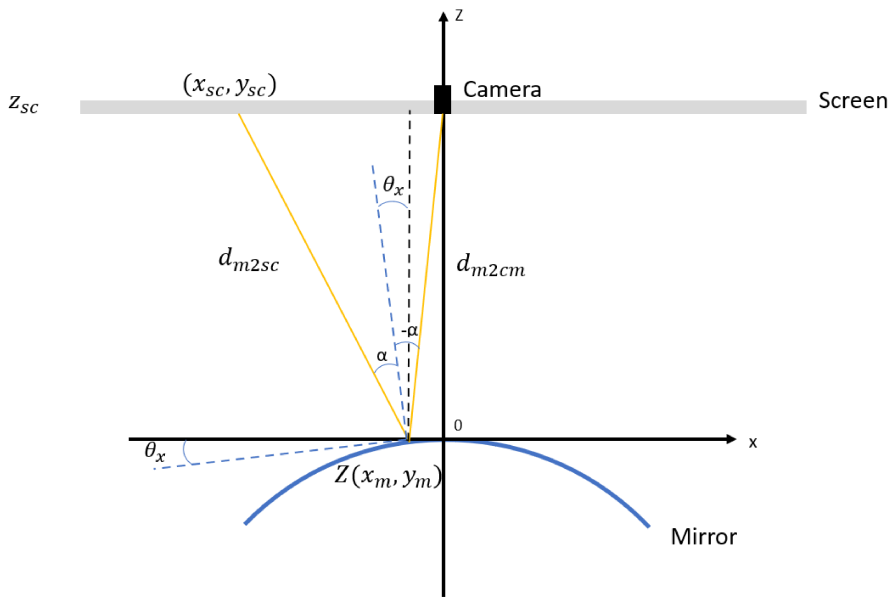

Figure 2. The configuration of the deflectometry measurement setup. Counterclockwise is positive for angles in this setup.

camera sits in the middle of the screens on one side and all face the mirror on the opposite end of the setup. A pixel on the screen lights up at (x_{sc}, y_{sc}), the light travels to the mirror at (x_m, y_m, z_m), where $z_m = Z(x_m, y_m)$ is dependent on the shape of the mirror, and gets reflected into the camera (x_c, y_c, z_c). In the case where the camera entrance is a pinhole, then there is a single ray that traces from the screen, to the mirror, and finally to the camera focal plane. The relationship between the coordinates on the screen, mirror, and camera for this

ray are given by the simple geometric and trigonometric functions below and there is a unique mapping between screen pixels and locations on the mirror.

$$tan(\theta_x - \alpha_x) = \frac{x_m - x_c}{L - Z(x_m, y_m)} \tag{1}$$

$$tan(\theta_x + \alpha_x) = \frac{x_m - x_s}{L - Z(x_m, y_m)}, \tag{2}$$

where L is the distance from the mirror vertex to the camera. Note that the equations above are for the surface slope in the x-direction. A similar set of equations exist for the y-direction. Changes in the mirror shape change the mapping of screen pixels to imaged pixels.

What we measure with deflectometry is the distortion of the projected image by the intervening mirror. The distorted image can be compared to an expected image (e.g. calculated knowing the location of the camera, screen, and mirror and the mirror expected shape). The shift in coordinates between the two gives us a measure of the x- and y- slopes of the mirror surface. Alternatively we can measure the change in the distorted image due to a change in the mirror shape (e.g. in response to the motion of an actuator on the ASM). In practice we need to extract screen pixel coordinates from the distorted image. Namely, we want to map each pixel in the camera image to a location on the mirror and to a location on the screen. The mirror location is relatively straight forward to extract. With the camera we image the mirror surface so apart from a possible image distortion due to the camera lens, the mirror location is directly extracted from the image of the mirror in the camera focal plane. To determine the corresponding screen pixel the most common approach is to display on the screen a sequence of sinusoidal patterns each with a known phase shift from the previous one. The sequence of images are analogous to the fringe patterns from a phase shifting interferometer but the screen pixel location (e.g. (x_s, y_s)) are encoded in the phase of the sine waves. The specific algorithm we have implemented in this project is the *Dual-frequency pattern scheme* proposed by Liu et al.[20] (2010).

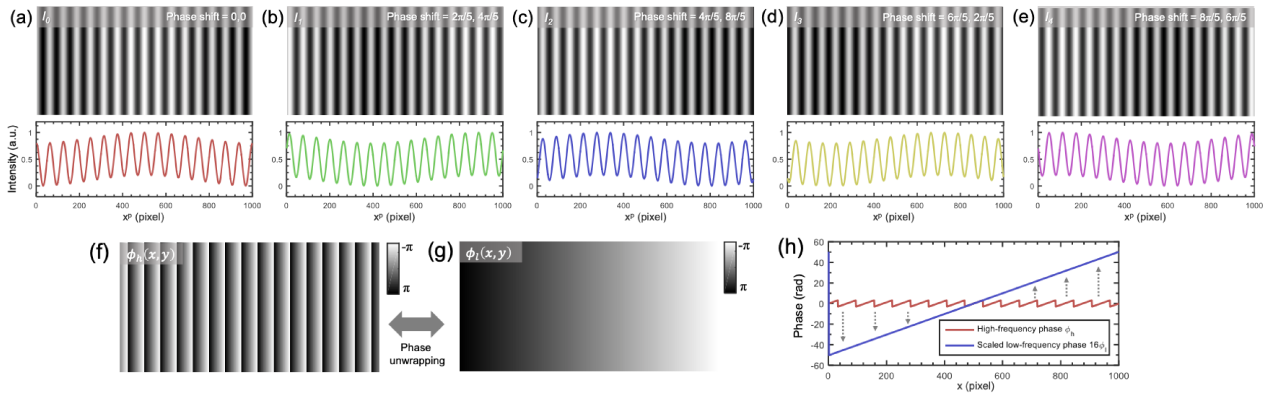

Figure 3. The dual-frequency pattern scheme and how it works to recover x- and y-positions of captured images. Only the set of "x-fringes" are shown but there is a similar set to extract the y positions. Image credit: Zuo et. al., 2018[21]

The *Dual-frequency pattern scheme* uses two groups of phase shifting patterns with sinusoidal functions with two different frequencies superimposed together. The high frequency patterns are for phase recovery with higher accuracy and the unit frequency patterns resolve the 2π ambiguity that exists during the phase unwrapping. The scheme is illustrated in Fig. 3.One set of the dual-frequency fringe patterns (five images) recover the absolute phase in one direction, so to get information for both the x and y directions, we need a set of vertical fringe patterns and a set of horizontal fringe patterns. A total of ten images gives us information of the mirror surface at one state. In the case of the actuator influence functions, we aim to make differential measurement of the ASM, so we first take a set of images with the mirror unperturbed as the reference wavefront, then another set with the mirror actuated or poked. The differential measurement pair would recover two sets of absolute phases Φ_x, Φ_y and Φ'_x, Φ'_y. By subtracting one set from another, we obtain the x- and y-coordinate shifts that can be

easily converted to x- and y-slopes induced by the mirror actuation using the functions

$$S_x(x,y) = \frac{(\Phi_x - \Phi'_x)\lambda_h}{2\pi * 2D(x,y)}, \tag{3}$$

$$S_y(x,y) = \frac{(\Phi_y - \Phi'_y)\lambda_h}{2\pi * 2D(x,y)}, \tag{4}$$

where λ_h is the wavelength of the projected high frequency patterns and D is the distance from the point on the mirror to the point on the screen. In conclusion, making one differential measurement requires twenty fringe images to be taken in total. The procedures for estimating the absolute surface shape of the ASM are the same as those for a differential measurement but instead of taking a set of fringe patterns for the reference wavefront, a set of calculated ideal images is used as the reference (e.g. using our ray-trace code). We only need to take one set of fringe images for an absolute measurement.

The above surface gradients are binned spatially and we then perform two-dimensional integration from slopes space to wavefront space via matrix multiplication. We use the standard Southwell geometry[22] to reconstruct the wavefront/surface shape.

3. RAY-TRACING SIMULATION

The above formalism was implemented in a simple ray tracing simulation to explore how deflectometry works and what kind of set up would be needed for the UH88 ASM. The simulation traces light backwards; a ray begins at the camera, intersects a particular location on the mirror, is reflected by the mirror, and then intersects at a location/pixel on the screen. Where the beam lands on the screen depends on the surface shape of the mirror and is described by Eq.(1) and (2). The simple ray-tracing simulation takes in parameters of the mirror surface shape, whether it be flat, convex, or concave, and the positions of the optical elements (e.g. the mirror, the screen, and the camera) and returns the expected mapping between the screen location and its corresponding mirror location that reflects the ray from the screen pixel into the camera. With this code, we can apply any aberrations we want on the mirror and we can inject errors into any of these parameters to test how these impact our ability to recover the known surface shape.

We studied two sources of errors that are relevant to the measurement of the influence functions: 1) instability of the positions of elements in the system (i.e. what happens when the camera or the screen moves position in between a differential measurement pair). Examples of this are dimensional variations due to changes in the temperature of the environment or vibrations in the system. 2) Misalignment of the components (e.g. what happens if the camera is off-axis rather than being on the optical axis of the ASM). We also used error injection to study how the absolute surface shape recovery depends on the errors in our knowledge of the setup (e.g. what happens when the assumed locations of the camera, mirror, and the screen are different from the actual locations).

Before performing any of the error injection tests, we first verified our ray-tracing code by comparing our ray-trace results for a variety of mirror shapes to the ray-trace solution from a commercial optical design program (Zemax). A random set of pixels on the screen are chosen to trace to the mirror and the camera using both our code and the Zemax model. We find that our ray-trace simulation and the Zemax ray-trace agree to better than 1% with most of the difference coming from an overall scale. Taking away the overall scale, the residual discrepancy is 0.07%. The source of the overall scale is not known but it could arise from simplifying assumptions in the Zemax ray-trace routines. An overall scale error leads to variations in the focus term of the recovered surface shape. This will limit our ability to recover the absolute radius of curvature of the mirror to about 1.5%, which is an acceptable error.

To test the positional tolerances of the setup, we studied how errors in the x-, y-, z-position of the camera and the z-position of the screen affect the recovered surface shape. First, we demonstrated that for differential measurements, errors in these parameters do not affect the reconstructed surface shape as long as they do not change between the reference and actuated measurements. Hence, the stability of the deflectometry setup is the most important factor. To quantify this stability requirement, we ran the ray-tracing simulation with known

aberrations applied (e.g. Zernike polynomials) to the mirror surface to calculated how much surface error is induced by a translation of the camera or the screen between a differential measurement.

Using the simulation code, we first make a differential measurement assuming perfect alignment of all of the components and no movement between measurements. This is our ideal estimate of the wavefront. We then make another differential measurement but one of the controllable parameters change by 100μm in between the differential measurement pair. The change of 100μm corresponds to the dimensional change of the setup due to a change in temperature of 6 degrees Celsius (not uncommon for our lab). The RMS error between the two reconstructed surface shapes is the our figure of merit. The RMS errors depends on the aberration we are trying to estimate (e.g. the surface of the mirror). The maximum RMS error induced by moving either the xyz position of the camera/screen by 100μm is 1.4% of the aberration applied to the mirror in the simulation; and it corresponds to the spherical term of the Zernike Polynomials. This error is well within the requirement we set for differential measurements, which is 10% as discussed in Section 1.2.

The second test we performed for PMD differential measurements using the simulation is to see how sensitive our estimate is on the placement of the camera along the optical axis of the ASM. We simulated taking differential measurements with the camera sitting at different locations on the xy-plane and compared the reconstructed wavefronts to the ideal wavefront measured with the camera being on-axis. The measurement is not sensitive to the camera placement and a wavefront error of 1% RMS is induced when the camera is ~100mm away from the optical axis.

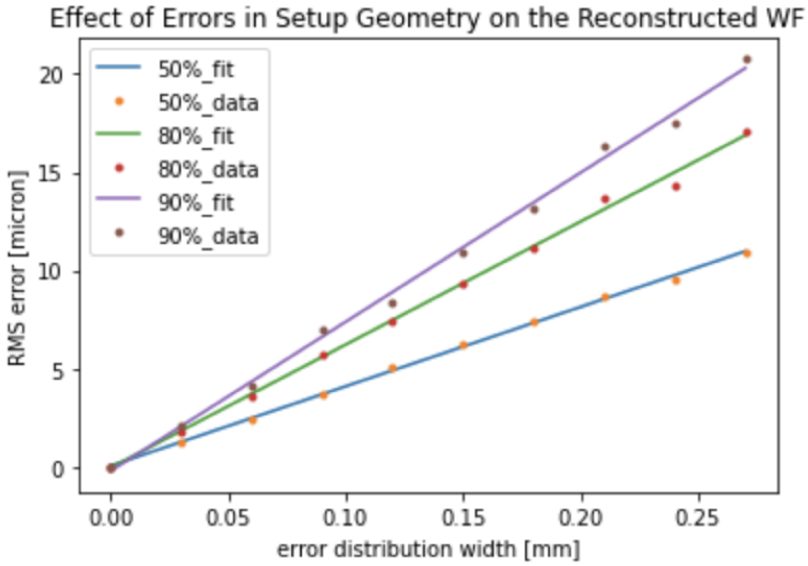

Figure 4. Given the requirement of measuring the absolute shape of the mirror with an accuracy down to a few microns, the graph shows that we need to know the positions of the optical elements (camera, mirror, and screen) with respect to each other well within 0.1mm.

The last experiment we did with the deflectometry simulation is quantifying how well we need to know the positions of the elements in the setup to make an absolute surface measurement to meet our requirement. As mentioned before, the requirement we set for an absolute measurement is a few microns. We used a Monte Carlo (MC) simulation in this test. During each iteration, some random errors are introduced to all four position parameter of the camera and the screen (e.g. x_c, y_c, z_c, and z_s). The random errors are drawn from a Gaussian distribution with a given standard deviation σ and an RMS surface error is computed from the reconstructed surface compared to the known input surface. 500 iterations were ran at each σ value and the result of the MC simulation is shown in Fig. 4. The three sets of data points and the three lines represent the median, the 80 percentile, and the 90 percentile errors. Note that the deviations of the data points from the fitted lines are caused by the limited number of iterations. Based on the figure, to measure the absolute mirror wavefront with less than a few microns RMS error we need to calibrate the geometric positions of the optics in the PMD

system accurate to less than 0.1mm error based on the 90 percentile error. This requirement will make obtaining absolute measurements of the surface difficult. Its similar to the stated positional accuracy of commercial hand-held metrology 3D scanning technologies and calibrations using a mirror with a known surface shape or multiple cameras may get us within this specification. We will perform this experiment with our future ASM setup.

Note that some setup features are not yet implemented in the ray-tracing simulation so their uncertainty effects have not been explored. Some important cases we still need to implement are the effect of tilting the screen with respect to the optical axis of the system and image distortion in the camera. Some of these, such as the tilt of the screen with respect to the mirror, may impact a differential measurements since it systematically shortens the screen in the direction of the tilt in both measurements. We plan to study their effects in the future.

4. LAB PROTOTYPE

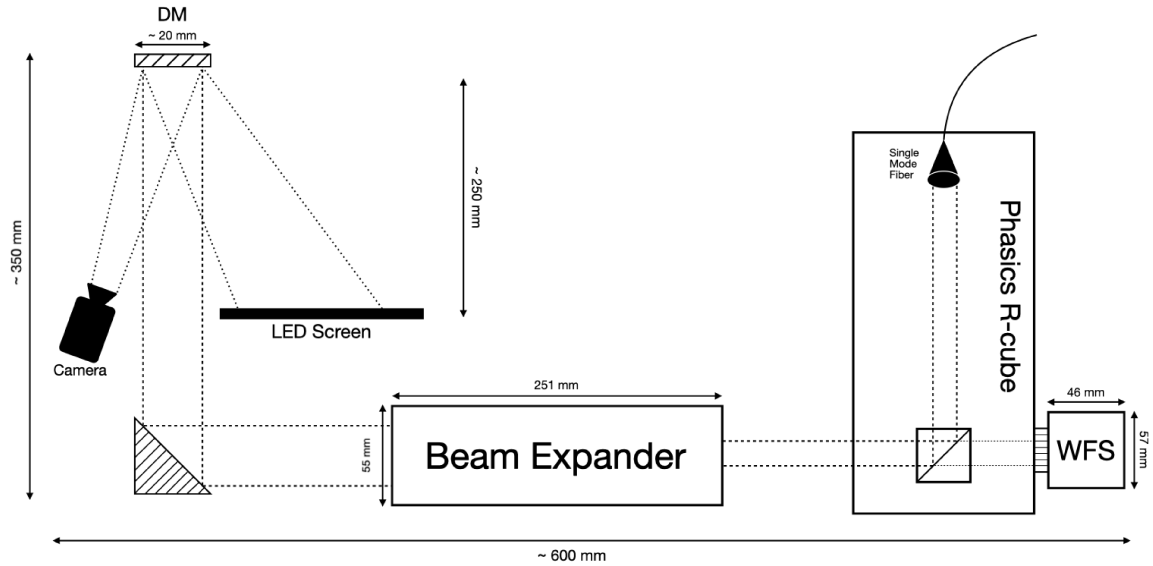

Figure 5. The designed layout of the prototype deflectometry setup with the Robo-AO DM.

To explore challenges with a real-world system we developed a lab prototype. The planned layout of the prototype is shown in Fig. 5. The blueprint contains two measurement setups: the PMD setup that includes the camera and the LED screen; and the Shack-Hartmann wavefront sensing setup that includes a beam expander, the Phasics R-cube, and the HASO wavefront sensor (WFS). The Shack-Hartmann wavefront sensing setup consists of commercial products that we planned to use as a reference for the PMD measurements. We only actualized the deflectometry setup, but we will add the Shack-Harmann WFS in the future.

The current prototype consists of Raspberry Pi computer with a 5.5-inch OLED screen, a Raspberry Pi HQ camera, and a 16mm focal length camera lens. The OLED screen is mounted into a custom mount that holds the screen on an optical post-mounted assembly. The camera and lens are mounted on a separate post and operate "off-axis" with respect to the screens. The surface under test is placed so that it reflects a portion of the screen(s) to the camera. The camera lens includes an iris and can be focused on either the mirror or the screen. An image of the prototype testing a small MEMS DM is shown in Figure 6.

The data acquisition (image display and image capture) is controlled by a python script that runs on the Raspberry Pi computer while the analysis and wavefront reconstruction is done by a separate computer. Images of the "fringe" patterns in both the x- and y- directions are taken separately along with a set of calibration images for background subtraction of ambient light and to correct for nonlinearities in the screen and camera. The data are obtained with the lab room lights off but there are various sources of light around the room that create a background ambient light level. These are removed using a background/"dark" calibration frame that is the average of a series of images taken with the screen illumination set to zero. The output of the screens and the

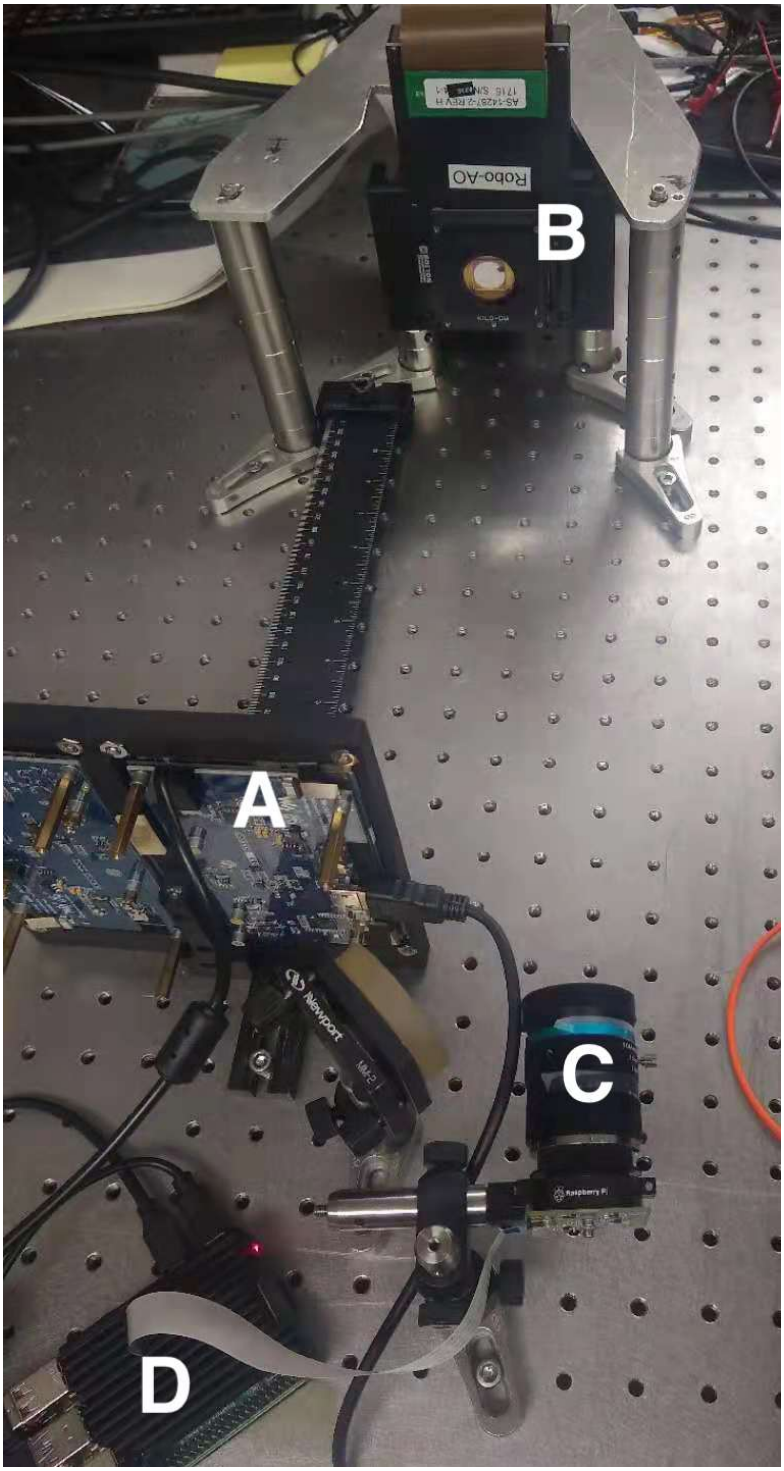

Figure 6. An image of the PMD prototype in the lab. A: LCD screen for fringe projection. B: the Robo-AO DM. C: Camera. D: Raspberry Pi that controls both the screen and the camera for data acquisition.

response of the imaging system have nonlinearities. We correct for these by illuminating the screen with a series of increasing brighter greyscale (red=green=blue) pixel intensities. At each grey scale level (e.g. 10%, 20%, ..., 100%) we construct an average background subtracted image in the camera. These images provide a correction lookup table to map the measured camera intensities into linear projected intensities. We linearly interpolate between points in the LUT but note that the nonlinearities are all at the extreme values (e.g. near zero or 255). The LUTs are done for each pixel in the camera. The PMD data frames (five fringe illuminations for x- and five for y-) are also averages of a number of individual frames. At the moment all data are taken 8-bit grayscale and the calibration and PMD data images are all taken at the same integration time ($t_{exp} \sim 100$ msec).

4.1 Tests with a Flat Mirror

To better understand deflectometry, we performed an experiment with the deflectometry setup using a 2 in. flat mirror. The setup is similar to Fig. 6 except instead of using the Robo-AO DM, a simple flat mirror is in place of B. In this small experiment, we wanted to verify the relationship between the distance D between the mirror and the screen/camera and our measurements follows Eq.(1) and Eq.(2). Hence, throughout the experiment, we kept the screen and the camera in the same location while moving the mirror closer each time by 50 mm($\sim$ 2 in.) starting at a distance of 343 mm (13.5 in.).

A square of a known size was projected on the screen, the square gets reflected off of the mirror and finally captured by the camera. Three sets of data were taken at distances of 343 mm, 293 mm, and 243 mm. As expected, when the distance between the mirror and the screen/camera decreases, the pixel size (i.e. the number of camera pixels it takes up) of the square in the images increases because objects subtend a larger angle when they are closer. On the other hand, since the mirror is flat, the physical size of the square that is projected on the mirror remains the same despite the varying distance D.

This means that the fringe pattern phase shifts caused by slopes on the surface of a mirror must be directly proportional to the distance D between the mirror and the screen/camera. Increasing D leads to increasing phase shift, and thus higher sensitivity. Therefore, in an ideal world with ideal screens and cameras (i.e. cameras and screens that have an infinite dynamic range and infinitely small pixel scale, etc.), we can increase the sensitivity of the PMD setup as much as we want by increasing the distance D. However, in the real world, we are limited by the pixels scale and dynamic range of the camera and the screen. There exists the trade-off of when D increases, the pixel size of the projected image gets smaller in the camera, thus worsens the camera's ability to accurately resolve the phase shifts. When designing the PMD setup for the ASM, we will perform the trade-off calculations between the distance D and the pixel scale of the camera to decide the optimal distance between the mirror and the screen/camera given the best camera we can work with.

4.2 Tests with a MEMS deformable mirror

The Robo-AO deflectometry setup is a fully operational system with a data acquisition routine and a data analysis pipeline. Fig. 6 shows how the Robo-AO deflectometry setup looks like on an optical bench. A Raspberry Pi controls the LCD screen that project the fringe patterns and the camera that captures the images reflected off of the DM. The Robo-AO DM has a round nominally flat mirror surface with a hexagonal active region that contains 492 actuators within a 9.2mm diameter. An example of a distorted fringe pattern reflected off of the Robo-AO DM is shown in Fig. 7. The DM had one actuator poked when the image was taken. The hexagonal active region is clearly visible, because the active actuators are placed at mid-range which creates a step between the active part of the mirror and the passive region. The poked actuator is actuator number 89 (shown in the image boxed by the white square) set to a different height from the other actuators. The cross section of a reconstructed wavefront zoomed onto where the actuator poked is shown in Fig. 8. The physical height of the reconstructed wavefront is currently arbitrary since we are still working on calculating the scaling relationship. One notable real-world issue we had to deal with was the non-linearity in the screen illumination, in the camera response, and any non-uniformity in the reflectivity of the mirror. We correct for all of these by taking calibration data including dark frames and flat-field/uniform illumination images in our data analysis pipeline.

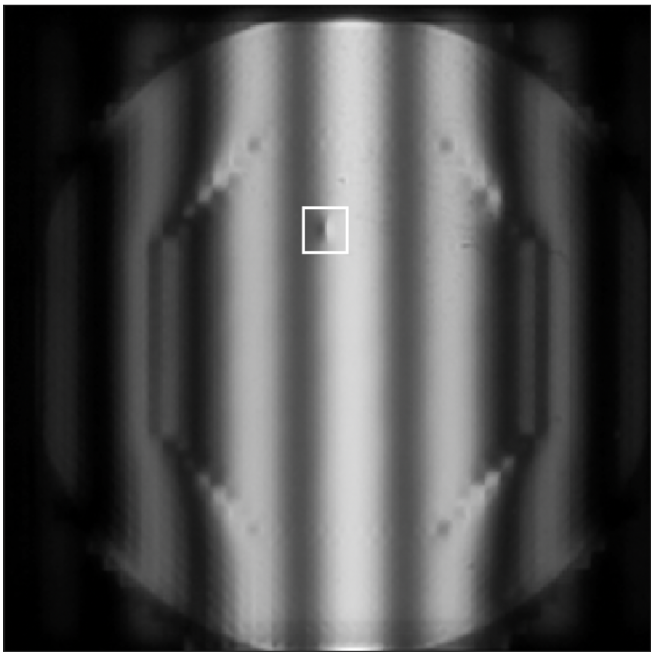

Figure 7. An example image of the deflected fringe patterns when an actuator on the DM is poked. The white box marks the poked actuator, which is number 89.

4.3 Effect of Exposure Time on Measurement Error

In reality, the iris of the camera is not a pinhole and there is a trade between more light/resolution by opening the iris on the camera and more depth of field (less sensitivity to focus errors) by closing down the iris. To quantify what exposure times are needed to collect the PMD measurements, we took datasets with exposure times varying from 75ms to 150ms while keeping the Robo-AO DM at a fixed state. More specifically, ten sets of data are taken at each exposure time setting, then the reconstructed wavefronts from those ten sets of data are compared with each other to calculate for an average RMS error within the set. The calculated RMS deviation is plotted as a function of exposure time in Fig. 9. The average RMS decreases during the range of 75ms to 100ms because the numbers of photons collected increase and also increases the SNR of the images. However, beyond 100ms, the curve flattens out which tells us that there is some other error that limits our precision. The remaining RMS error may be due to the limited dynamic range of the camera (8-bits) but we have not tried a higher resolution camera yet.

We note that the measured variations are already well below our measurement requirement of 1μm for differential measurements so we conclude that at least for the current setup the LCD screens and the relatively short exposure times will meet our requirements.

4.4 Focus of the PMD Setup

The second aspect of the camera iris is that opening the iris reduces the depth of focus so the camera can only be in focus for either the mirror or the screen. We made a series of measurements of the Robo-AO DM with a single actuator poked up but varying the location where the camera was focused. Based on results of the setup prototype, the answer is clear - the camera must be focused on the mirror. When the camera focuses on the screen(s), the fringes patterns are in focus, but we lose spatial resolution at the mirror. In some cases this blurring can be so severe that the reconstructed wavefront looks nothing like a poked actuator. On the other hand, when the camera focuses on the mirror, the fringe patterns are out of focus. However, this does not affect the measured phase of the sinusoidal fringe pattern and therefore does not affect our ability to map the screen pixels to the mirror coordinates. This is consistent with what others have found[15] and one of the motivations for using sinusoidal patterns.

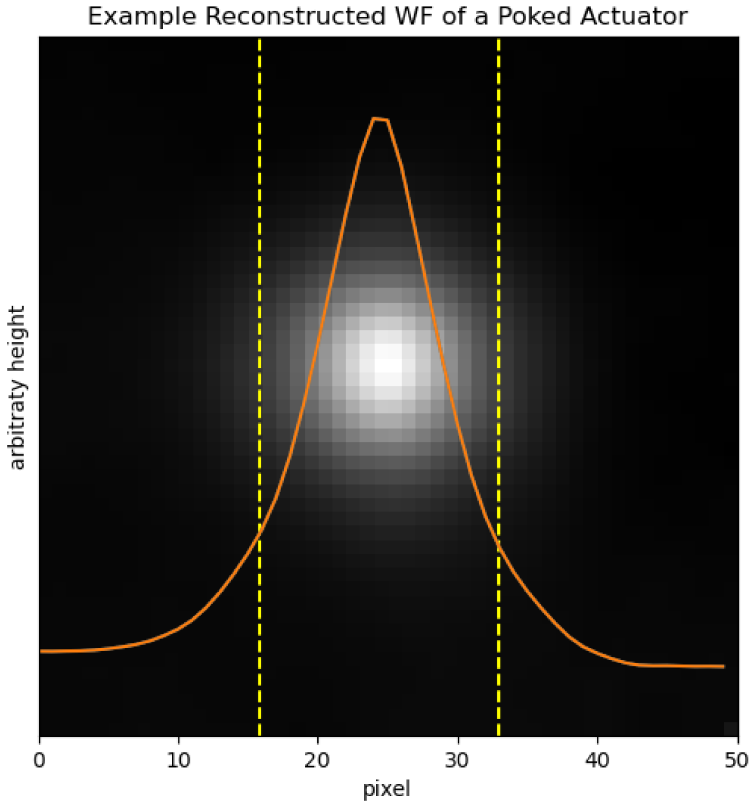

Figure 8. Cross sectional view of a reconstructed wavefront zoomed-in on a poked actuator plotted on top of its 2D wavefront image as the orange curve. The yellow lines mark where the neighboring actuators are at, and they show that there is an inter-actuator coupling of about 20%.

Focusing the camera on the mirror surface helps to maintain the spatial resolution on the mirror and in the recovered influence functions. Achieving a good focus and high spatial resolution is related to the iris size of the camera and the image quality of the lens. Stopping down the reduces the effect of lens aberrations and increases the depth of focus. However, a small aperture on the camera reduces the angular resolution of the system. For our system we find that as the iris opens larger, the resolution of the images improves, but this trend stops when the iris reaches a certain size. We expect that at this point aberrations in the relatively inexpensive Raspberry Pi camera lens or in the detector are the limitations. However, as demonstrated in Figure 8, the resolution is sufficient for these lab tests.

4.5 Systematic Drift

The last property explored using the lab-setup is the systematic drift of the PMD setup over a period of time. We took five sets of data of the mirror under the same state over a time period of one hour and compared the RMS differences between the data sets. The results are shown in Fig. 10. The data sets shown in the figure were taken when actuator number 89 of the Robo-AO DM is set to a relative position of 1.0 whereas the rest of the active region remains at position 0.5 as shown in Fig. 7, where position 1.0 is when the actuator is fully actuated and 0.0 being at the original position. As expected, the longer the time is between two measurements, the larger the RMS error.

One caveat of this experiment is we cannot differentiate how much of the drift is caused by the deflectometry setup and how much of the drift is caused by the DM itself. Additionally, this experiment only spanned a time

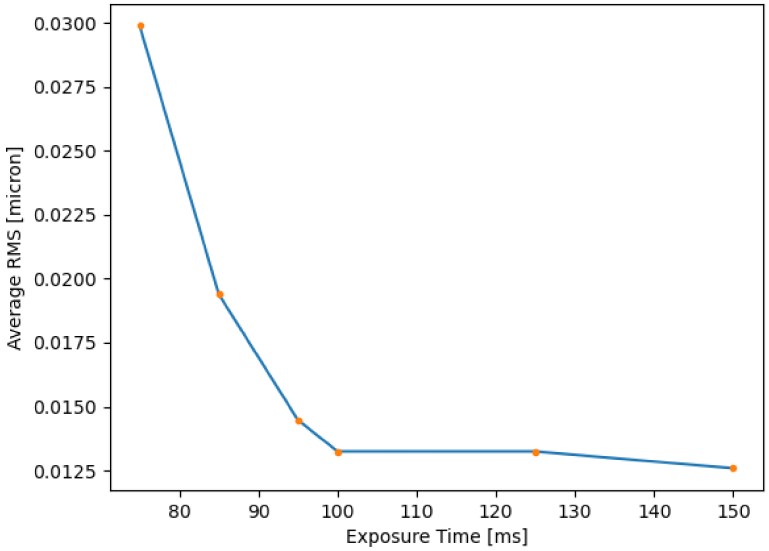

Figure 9. At short exposure times, increasing the exposure time decreases the RMS error between measurements, but this effect plateaus at 100ms. This shows that the PMD system is not photon-limited but is constrained by other systematic effects.

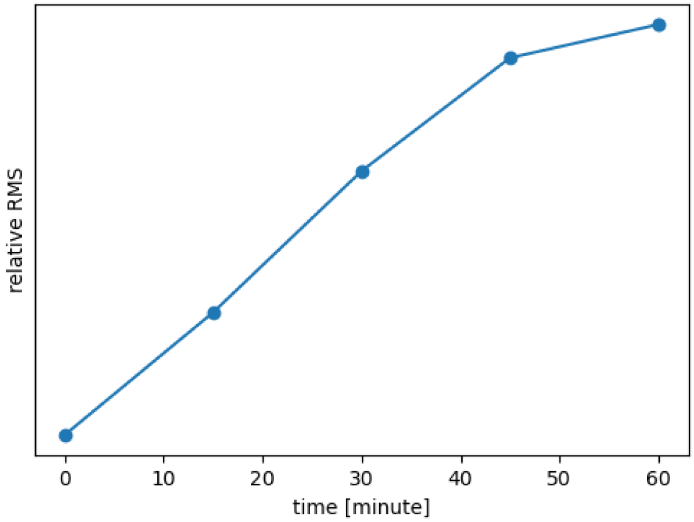

Figure 10. The average variation between five sets of PMD measurements on the prototype setup taken with no change in the system over the course of an hour.

period of one hour; it does not tell us how the drift changes over a longer period of time. In the future, we plan to investigate this deeper with the ASM deflectometry setup by taking data over a longer span of time to examine whether we need to correct for this error or not. With the existing data taken with the setup prototype, a drift of 0.06μm over a one-hour period meets the differential measurement requirement of keeping the measurement error less than 0.1μm.

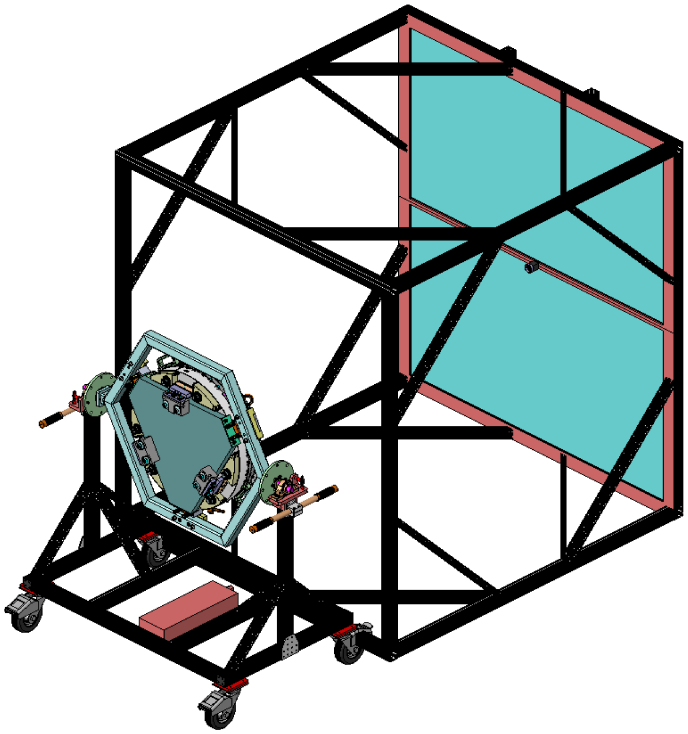

Figure 11. The preliminary CAD rendering of the ASM PMD setup. Image credit: Alan Ryan.

5. PRELIMINARY DESIGN OF THE ASM DEFLECTOMETRY SETUP

The setup prototype with the Robo-AO DM mets the basic requirements that we have set for differential PMD measurements for the type of lab measurements we need for the ASM. The ray-tracing simulation also gave us guidance on how we should design the ASM PMD setup. In this section we discuss the basic layout of a PMD setup for testing the UH88 ASM. A preliminary CAD rendering of the ASM PMD setup is shown in Fig. 11. The ASM is secured onto its handling cart via a triangular supporting structure and a rotating hexagonal frame. The cart will interface with a larger structure that contains two large LCD TV screens and a camera mounted to the middle of the two screens. The distance between the apex of the ASM and the screens is set to be 2m. The fringe pattern, displayed on the two screens gets reflected off of the ASM into the camera (shown schematically as the small black cylinder in the figure).

The UH88 ASM is an aspherical convex mirror with a diameter of 620mm, a radius of curvature R of -4198mm, and with a conic constant k of -3.604. The shape of the facesheet is described by the equation

$$Z_m(x_m, y_m) = \frac{R + \sqrt{R^2 - (x^2 + y^2) - k(x^2 + y^2)}}{1 + k}. \tag{5}$$

Given the parameters above and Eq. (1), (2), and (5), we calculated the screen size required to perform PMD measurements for the UH88 ASM needs to cover an area on the screen of diameter 930mm. In the test setup we achieve this using two 75-inch LCD screens. The code written for the prototype that performs the data acquisition and the data analysis can be easily generalized to control the ASM system. Currently, the data acquisition, data analysis, and DM commands are three separate processes on three different computers for the prototype. With the ASM setup, we will integrate the process into a single control computer.

6. CONCLUSION AND DISCUSSION

As a result of this project we plan to construct a PMD setup for the UH88 ASM project. Challenges remain to demonstrate that PMD for large convex ASMs can achive the ¡ 1μm accuracy. However our initial results are

promising. We find that we do not need very sophisticated components for the implementation though we see limitations from the very simple camera and camera lens used in the prototype system. An improved camera and camera lens are already being acquired for the next set of tests. In addition, the basic stability requirements and the required metrology of the PMD setup have been quantified. Key challenges remaining to be explored include quantifying how variations in the system (e.g. tilts or deformations of the screens) impact the recovered influence functions.

ACKNOWLEDGMENTS

We acknowledge the NSF award 1910552 that funded this project. We would also like to thank the UH Robo-AO team for lending us the Robo-AO DM and using the Robo-AO lab space. Thanks to Christoph Baranec and Paul Barnes for teaching us how to work with the DM. Finally, we would like to thank Alan Ryan, our mechanical engineer, for helping us with the preliminary design of the UH88 ASM PMD setup.

REFERENCES

[1] Davies, R. and Kasper, M., "Adaptive Optics for Astronomy," *Annual Review of Astronomy and Astrophysics* **50**, 305–351 (Sept. 2012).

[2] Riccardi, A., Brusa, G., Salinari, P., Gallieni, D., Biasi, R., Andrighettoni, M., and Martin, H. M., "Adaptive secondary mirrors for the Large Binocular Telescope," in [*Adaptive Optical System Technologies II*], Wizinowich, P. L. and Bonaccini, D., eds., *Society of Photo-Optical Instrumentation Engineers (SPIE) Conference Series* **4839**, 721–732 (Feb. 2003).

[3] Arsenault, R., Biasi, R., Gallieni, D., Riccardi, A., Lazzarini, P., Hubin, N., Fedrigo, E., Donaldson, R., Oberti, S., Stroebele, S., Conzelmann, R., and Duchateau, M., "A deformable secondary mirror for the VLT," in [*Advances in Adaptive Optics II*], Ellerbroek, B. L. and Calia, D. B., eds., **6272**, 284 – 295, International Society for Optics and Photonics, SPIE (2006).

[4] Lloyd-Hart, M., "Thermal performance enhancement of adaptive optics by use of a deformable secondary mirror," *Publications of the Astronomical Society of the Pacific* **112**(768), 264–272 (2000).

[5] Briguglio, R., Quiros-Pacheco, F., Males, J. R., Xompero, M., Riccardi, A., Close, L. M., Morzinski, K. M., Esposito, S., Pinna, E., Puglisi, A., Schatz, L., and Miller, K., "Optical calibration and performance of the adaptive secondary mirror at the Magellan telescope," **8**, 10835, Scientific Reports (2018).

[6] Roddier, F. J., Cowie, L. L., Graves, J. E., Songaila, A., McKenna, D., Vernin, J., Azouit, M., Caccia, J. L., Limburg, E. J., Roddier, C. A., Salmon, D. A., Beland, S., Cowley, D. J., and Hill, S., "Seeing at Mauna Kea: a joint UH-UN-NOAO-CFHT study," in [*Advanced Technology Optical Telescopes IV*], Barr, L. D., ed., *Society of Photo-Optical Instrumentation Engineers (SPIE) Conference Series* **1236**, 485–491 (July 1990).

[7] Marks, R. D., Vernin, J., Azouit, M., Briggs, J. W., Burton, M. G., Ashley, M. C.B., and Manigault, J. F., "Antarctic site testing - microthermal measurements of surface-layer seeing at the south pole," *Astron. Astrophys. Suppl. Ser.* **118**(2), 385–390 (1996).

[8] Chun, M., Wilson, R., Avila, R., Butterley, T., Aviles, J.-L., Wier, D., and Benigni, S., "Mauna Kea ground-layer characterization campaign," *Monthly Notices of the Royal Astronomical Society* **394**, 1121–1130 (04 2009).

[9] Szeto, K., Andersen, D., Crampton, D., Morris, S., Lloyd-Hart, M., Myers, R., Jensen, J. B., Fletcher, M., Gardhouse, W. R., Milton, N. M., Pazder, J., Stoesz, J., Simons, D., and Véran, J.-P., "A proposed implementation of a ground layer adaptive optics system on the Gemini Telescope," in [*Society of Photo-Optical Instrumentation Engineers (SPIE) Conference Series*], McLean, I. S. and Iye, M., eds., *Society of Photo-Optical Instrumentation Engineers (SPIE) Conference Series* **6269**, 626958 (June 2006).

[10] Minowa, Y., Koyama, Y., Ono, Y., Tanaka, I., Hattori, T., Clergeon, C., Akiyama, M., Kodama, T., Motohara, K., Rigaut, F., d'Orgeville, C., Wang, S.-Y., and Yoshida, M., "ULTIMATE-Subaru: enhancing the Subaru's wide-field capability with GLAO," in [*Advances in Optical Astronomical Instrumentation 2019*], *Society of Photo-Optical Instrumentation Engineers (SPIE) Conference Series* **11203**, 112030G (Jan. 2020).

[11] Christou, J. C., Brusa, G., Guerra, J. C., Lefebvre, M., Miller, D., Rahmer, G., Sosa, R., and Wagner, M., "Living with adaptive secondary mirrors 365/7/24," in [*Adaptive Optics Systems IV*], Marchetti, E., Close, L. M., and Vran, J.-P., eds., *Society of Photo-Optical Instrumentation Engineers (SPIE) Conference Series* **9148**, 91480F (Aug. 2014).

[12] Chun, M. R., Ryan, A., Zhang, R., Kuiper, S., Ackaert, G., Baranec, C., Baeton, M., Bos, A., Bowens-Rubin, R., Dekker, B., Dungee, R., Gupta, T., Hinz, P., Jonker, W., Kamphues, F., Lai, O., Lu, J., Maniscalco, M., Monna, B., Nair, M., Nigenhuis, J., Priem, H., and Vogel, P.-A., "Progress on the University of Hawaii 2.2-meter adaptive secondary mirror," *Society of Photo-Optical Instrumentation Engineers (SPIE) Conference Series* (2022).

[13] Jonker, W. A., Vogel, P.-A., Horst, R. t., Vu, A. T., Kuiper, S., and Kamphues, F., "Hot forming of a large deformable mirror facesheet," *Society of Photo-Optical Instrumentation Engineers (SPIE) Conference Series* (2022).

[14] Kuiper, S., Jonker, W. A., Maniscalco, M., van der Ven, E., Voorhoeve, R., Chun, M., Lai, O., and Lu, J., "Performance analysis of the adaptive secondary mirror for the UH2.2 telescope," in [*Adaptive Optics Systems VII*], Schreiber, L., Schmidt, D., and Vernet, E., eds., **11448**, 1146 – 1154, International Society for Optics and Photonics, SPIE (2020).

[15] Huang, L., Idir, M., Zuo, C., and Asundi, A., "Review of phase measuring deflectometry," *Optics and Lasers in Engineering* **107**, 247–257 (2018).

[16] Arsenault, R., Madec, P.-Y., Paufique, J., La Penna, P., Stroebele, S., Vernet, E., Pirard, J.-F., Hackenberg, W., Kuntschner, H., Kolb, J., Muller, N., Le Louarn, M., Amico, P., Hubin, N., Lizon, J.-L., Ridings, R., Abad, J., Fischer, G., Heinz, V., Kiekebusch, M., Argomedo, J., Conzelmann, R., Tordo, S., Donaldson, R., Soenke, C., Duhoux, P., Fedrigo, E., Delabre, B., Jost, A., Duchateau, M., Downing, M., Moreno, J., Manescau, A., Bonaccini Calia, D., Quattri, M., Dupuy, C., Guidolin, I., Comin, M., Guzman, R., Buzzoni, B., Quentin, J., Lewis, S., Jolley, P., Kraus, M., Pfrommer, T., Garcia-Rissmann, A., Biasi, R., Gallieni, D., and Stuik, R., "The ESO Adaptive Optics Facility under Test," in [*Proceedings of the Third AO4ELT Conference*], Esposito, S. and Fini, L., eds., 118 (Dec. 2013).

[17] Huang, R., *High precision optical surface metrology using deflectometry*, PhD thesis, University of Arizona (Jan. 2015).

[18] Noll, R. J., "Zernike polynomials and atmospheric turbulence.," *Journal of the Optical Society of America (1917-1983)* **66**, 207–211 (Mar. 1976).

[19] Bowens-Rubin, R., Hinz, P., Kuiper, S., and Dillon, D., "Performance of large-format deformable mirrors constructed with hybrid variable reluctance actuators II: initial lab results from FLASH," in [*Techniques and Instrumentation for Detection of Exoplanets X*], Shaklan, S. B. and Ruane, G. J., eds., **11823**, 554 – 573, International Society for Optics and Photonics, SPIE (2021).

[20] Liu, K., Wang, Y., Lau, D. L., Hao, Q., and Hassebrook, L. G., "Dual-frequency pattern scheme for high-speed 3-d shape measurement," *Opt. Express* **18**, 5229–5244 (Mar 2010).

[21] Zuo, C., Feng, S., Huang, L., Tao, T., Yin, W., and Chen, Q., "Phase shifting algorithms for fringe projection profilometry: A review," *Optics and Lasers in Engineering* **109**, 23–59 (2018).

[22] Southwell, W. H., "Wave-front estimation from wave-front slope measurements," *Journal of the Optical Society of America (1917-1983)* **7**, 998 (Aug. 1980).